

Wide Spectrum Terahertz-Wave Generation From Nonlinear Waveguides

Kei Takeya, Koji Suizu, Hironobu Sai, Toshihiko Ouchi, and Kodo Kawase, *Member, IEEE*

(Invited Paper)

Abstract—We have obtained efficient terahertz (THz)-wave generation from surface-emitting or waveguide propagation using Cherenkov-type radiation with nonlinear optical (NLO) crystals. This approach presented the following advantages: 1) many crystals can be used as THz-wave emitters; 2) it is not necessary to satisfy the phase-matching condition inside the crystal; and 3) THz-wave generation is not suppressed by the absorption in the crystal. We demonstrated that the THz-wave generation was enhanced $50\times$ by suppressing the phase mismatch with a surfing configuration for bulk lithium niobate (LiNbO_3) crystals. Using the prism-coupled Cherenkov phase-matching method with organic crystal 4-dimethylamino-N-methyl-4-stilbazolium tosylate, we produced tunable THz radiation within $\sim 0.1\text{--}10$ THz. There was no evidence of significant absorption in the crystal. To show the advantages of the waveguide emitter, we demonstrated THz generation using a ridge-type LiNbO_3 waveguide with a thickness of $3.8\text{ }\mu\text{m}$. We obtained THz-wave generation with an ideal temporal half-cycle pulse and a wide tuning range, which is applied to reflection tomography imaging.

Index Terms—Cherenkov phase matching, LiNbO_3 , terahertz (THz), waveguide.

I. INTRODUCTION

RECENT advances in the field of terahertz (THz) technology, corresponding to frequencies in the range of $0.1\text{--}10$ THz, are remarkable and essential to new developments in the areas of imaging, diagnostics, microelectronics, and spectroscopy [1], [2]. A THz emitter consists of a photoconductive antenna (PCA) and a nonlinear optical (NLO) crystal. NLO crystals, such as 4-dimethylamino-N-methyl-4-stilbazolium tosylate (DAST), LiNbO_3 , LiTaO_3 , and GaAs, are used as effective THz sources based on their second-order nonlinearity [3]–[27]. Various studies have been carried out on THz gen-

eration from NLO crystals using parametric processes [3]–[7], difference frequency generation (DFG) [8]–[11], optical rectification [12]–[16], and coherent phonon emission [17]–[19].

Effective THz generation, however, is suppressed by the high absorption coefficient of the NLO crystals. Because the refractive index of NLO crystals is different for optical and THz frequencies, the phase-matching conditions and the coherent length for optical rectification are issues for effective THz generation. In this study, we have addressed these issues by developing a method for efficient THz-wave generation that is based on surface-emitting or waveguide propagation with Cherenkov-type radiation using NLO crystals [20]–[27]. This method has the following advantages: 1) since the THz wave is generated on the crystal surface, the absorption is minimized and 2) the phase-matching condition is relaxed using a suitable cladding material.

II. THZ GENERATION USING CHERENKOV PHASE MATCHING

A. Principles of Cherenkov Phase Matching

When the velocity of the polarization wave inside the NLO crystal is greater than the velocity of the generated wave outside the crystal, the Cherenkov phase-matching condition is satisfied. The radiation angle θ is determined by the group-refractive index of the pumping wave in the crystal n_g and that of the THz wave in the crystal n_{THz} [12], [28]

$$\cos \theta = \frac{\lambda_{\text{THz}}/n_{\text{THz}}}{2L_c} = \frac{n_g}{n_{\text{THz}}} \quad (1)$$

where λ_{THz} is the wavelength of the contributing waves and L_c is the coherence length of the surface-emitted wave. The value of n_{THz} should be larger than n_g from (1). The LiNbO_3 crystal has a refractive index of ~ 2.1 in the near-infrared region; its value is ~ 5.1 for THz frequencies. The generated THz wave is totally reflected at the air– LiNbO_3 interface. Using a silicon (Si) layer, the total internal reflection at this interface can be canceled (see Fig. 1.)

The radiation angle hardly changes during THz-frequency tuning because the refractive-index dispersion of Si is low in the THz-frequency range [29]; thus, the optical wavelength required only slight tuning. The change in the radiation angle is less than 0.01° for a fixed pump wavelength. The actual change in the radiation angle for the THz wave was significantly better than that for a THz parametric oscillator (TPO) with a Si-prism coupler [30], which experienced a change of $\sim 1.5^\circ$ over the $0.7\text{--}3.0\text{-THz}$ tuning range.

Manuscript received May 1, 2012; revised June 25, 2012; accepted June 29, 2012. Date of publication August 3, 2012; date of current version February 1, 2013. This work was supported in part by a Grant-in-Aid for Scientific Research (B) and the Japan Science and Technology Agency.

K. Takeya is with the Department of Electrical Engineering, Nagoya University, Nagoya 464-8603, Japan (e-mail: takeya@nuee.nagoya-u.ac.jp).

K. Suizu is with the Department of Electrical, Electronics and Computer Engineering, Chiba Institute of Technology, Narashino, Chiba 275-0016, Japan (e-mail: suizu.koji@it-chiba.ac.jp).

H. Sai and T. Ouchi are with the Canon Inc., Ohta-ku, Tokyo 146-8501, Japan (e-mail: ouchi.toshihiko@canon.co.jp).

K. Kawase is with the EcoTopia Science Institute, Nagoya University, Nagoya 464-8603, Japan, and also with RIKEN, Sendai 980-0845, Japan (e-mail: kawase@nuee.nagoya-u.ac.jp).

Color versions of one or more of the figures in this paper are available online at <http://ieeexplore.ieee.org>.

Digital Object Identifier 10.1109/JSTQE.2012.2209175

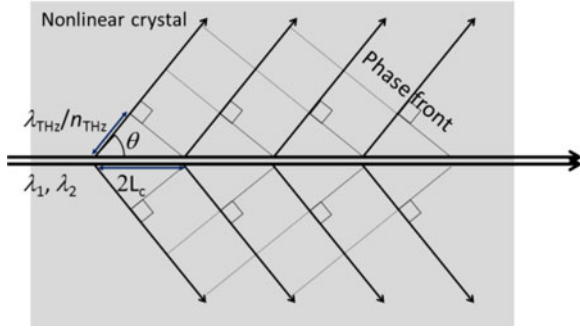


Fig. 1. Schematic of Cherenkov phase-matched monochromatic THz-wave generation. The phase-matching condition is satisfied when $2L_c = \lambda_{\text{THz}}/n_{\text{THz}}$.

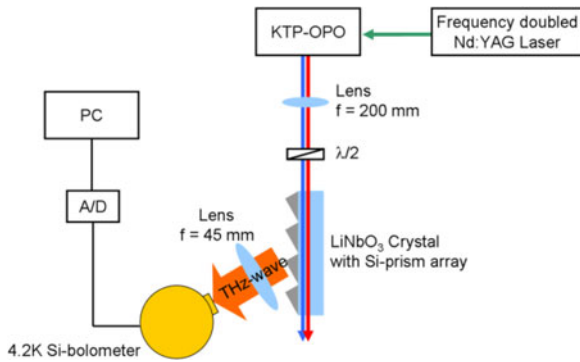


Fig. 2. Experimental setup for Cherenkov phase-matching monochromatic THz-wave generation.

B. Cherenkov Phase-Matched Monochromatic THz-Wave Generation

Using the experimental setup shown in Fig. 2, the method described in the aforementioned section was demonstrated. A frequency-doubled neodymium: YAG laser (repetition rate: 50 Hz, pulse energy: 12 mJ for 532 nm operation, pulse duration: 15 ns) was used as the pump source for a dual-wavelength potassium–titanium–oxide phosphate (KTP) optical parametric oscillator (OPO). The KTP OPO, which consisted of two KTP crystals with independently controlled angles, was capable of dual-wavelength operation with independent tuning of each wavelength [31], [32]. The OPO had a tunable range of 1300–1600 nm. The maximum output energy obtained was 2 mJ for pump energy of less than 12 mJ. The 5 mol% MgO-doped lithium niobate crystal (MgO:LiNbO₃) used in the experiment was cut from a $5 \times 65 \times 6$ -mm wafer, and the x -surfaces at both ends of the crystal were mirror polished. An array of seven Si-prism couplers was placed on the y -surface of the MgO:LiNbO₃ crystal. The y -surface was also mirror polished to minimize the coupling gap between the prism base and the crystal surface and to prevent scattering of the pump beam, which excites free carriers at the Si-prism base. The diameter of a pump beam was reduced to increase the power density. The polarizations of the pump and THz waves were both parallel to the z -axis of the crystals. The THz-wave output was measured with a fixed 4-K Si bolometer.

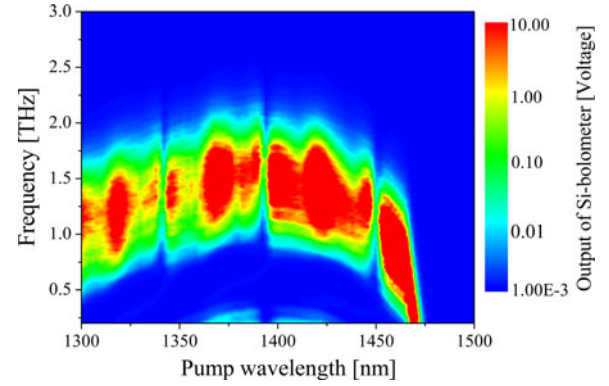


Fig. 3. THz-wave output mapping for various pump wavelengths and corresponding THz-wave frequencies. The x -axis and y -axis denote the pump wavelength λ_1 and the THz-wave frequency, respectively. The magnitude of the map values indicates the output voltage of the detector. The blue, green, and red curves are contour plots corresponding to the detector output voltages of 10 mV, 100 mV, and 1 V, respectively.

Fig. 3 shows the THz-wave frequencies for various pumping wavelengths and the corresponding THz-wave output mapping. The amplitude of the map denotes the output voltage of the Si bolometer with a gain of 200. The noise level of the bolometer was ~ 10 mV and is shown as the blue region in Fig. 3. The green and red parts show the regions of 100 mV and 1 V of output voltage, respectively. The blue, green, and red curves are contour plots for 10 mV, 100 mV, and 1 V, respectively. By choosing the proper pump wavelength, wide tunability over a range of 0.2–3.0 THz was achieved (Fig. 3). For frequencies below 1.0 THz, the pumping efficiency was improved significantly compared with our previous TPO systems pumped by 1470 nm.

The actual value of THz-wave output energy was estimated following $10 \text{ V} \approx 110 \text{ pJ pulse}^{-1}$ for low-repetition rate detection, an amplifier gain of 200 at the bolometer, and the pulsed heating of the Si device. The highest THz-wave energy obtained was $\sim 80 \text{ pJ}$; the energy-conversion efficiency from the λ_1 wave (1 mJ pulse^{-1}) was $\sim 10^{-5} \%$. In spite of the low excitation energy of only 1 mJ, this value is nearly equal to that of the former TPO system. THz-wave output energy has the strong dependence on the pump wavelength (Fig. 3). For 0.8-THz-wave generation, the output energy had a dip at a pump wavelength of ~ 1400 nm. We obtained extremely high energy in the low-frequency region below 0.3 THz (millimeter-wave region) using 1470-nm pumping. The dispersion of the pumping waves cannot explain these results; thus, an explanation is left for future research. However, we were able to produce a flat output spectrum over a range of 0.2–2.0 THz by varying the pump wavelength.

Cherenkov phase matching inherently requires a waveguide structure for nonlinear polarization to suppress phase mismatch in the direction perpendicular to the guiding mode (i.e., normal to the crystal surface) [28]. We can cancel the phase mismatch in the direction of THz-wave propagation, if we reduce the pump-beam width in that direction to about one-half of the THz wavelength (i.e., $\sim 10 \mu\text{m}$ for 3-THz waves) considering the refractive index of MgO:LiNbO₃ in the THz-wave region [33]. In this case, the waist of the pump beam in MgO:LiNbO₃ was $\sim 300 \mu\text{m}$,

which corresponded to five cycles of 1.0-THz waves and one cycle of 2.0-THz waves. Although the experimental conditions did not satisfy the requirement for Cherenkov phase matching, we successfully detected Cherenkov-radiated THz waves, which originated from the higher absorption area of the crystal. THz waves generated far from the crystal surface were attenuated, and no significant phase mismatch occurred. Furthermore, by shaping the pump beams with a focused cylindrical lens or by adopting the waveguide structure of the crystal [34], we minimized the phase-match condition and obtained greater power density of the pump beams, which resulted in higher conversion efficiency. The results obtained from using the waveguide structure of the crystal are described in a later section.

C. THz-Wave Generation With Surfing Configuration for Bulk LiNbO₃ Crystals

To suppress the phase-match limitations, we used a “surfing” configuration of the Cherenkov-type THz-wave generation with bulk crystals. In this configuration, dual wavelength beams were combined within a finite angle to produce an interference pattern of the pump waves in the crystal, which in turn, produced second-order nonlinear polarization for the THz frequencies. The interference pattern produced by the difference frequency of the dual wavelength beams was superimposed over the checkerboard interference pattern [35] produced by the interference of angled beams with the same frequency.

Fig. 4 shows the electric field distribution of (a) the pumping waves and (b) the excited nonlinear polarization, with $\lambda_1 = 1300$ nm and $\lambda_2 = 1317$ nm [where the DFG interaction $\omega_1 = \omega_2 - \omega_{\text{THz}}$, the corresponding THz frequency is 3 THz, and α represents the angle between the divided pump beams ($\alpha = 3.7^\circ$)]. The following (2) presents the periods A for the x -axis and B for the y -axis of the nonlinear polarization patterns of the dual-wavelengths beams

$$\begin{aligned} A &= \frac{2\pi}{(k_1 - k_2) \cos \frac{\alpha}{2}} \\ B &= \frac{4\pi}{(k_1 + k_2) \sin \frac{\alpha}{2}} \end{aligned} \quad (2)$$

where $k_1 = 2\pi n_1/\lambda_1$ and $k_2 = 2\pi n_2/\lambda_2$; here, n_1 and n_2 are the refractive indices for λ_1 and λ_2 , respectively. We used the Sellmeier equation in the near-infrared region for the LiNbO₃ crystal [36]. The Cherenkov angle of the crystal θ_c is determined from the crystal length A and the THz wavelength in the crystal, $C = \lambda_{\text{THz}}/n_{\text{THz}}$; here, λ_{THz} and n_{THz} correspond to the THz wavelength in vacuum and the refractive index of the crystal at the THz frequency, respectively. The proper angle α for the pump beams corresponding to the required THz frequency allows the satisfaction of the phase-matching condition for the direction of THz-wave propagation. The angle α is formulated from the geometric relation of A , B , and C , where $A^2 C^2 + B^2 C^2 = A^2 B^2$, as shown in Fig. 4(c):

$$\alpha = 2 \arccos \left(\sqrt{\frac{-(k_1 + k_2)^2 + \frac{16\pi^2}{(\lambda_{\text{THz}}/n_{\text{THz}})^2}}{4(k_1 - k_2)^2 - (k_1 + k_2)^2}} \right). \quad (3)$$

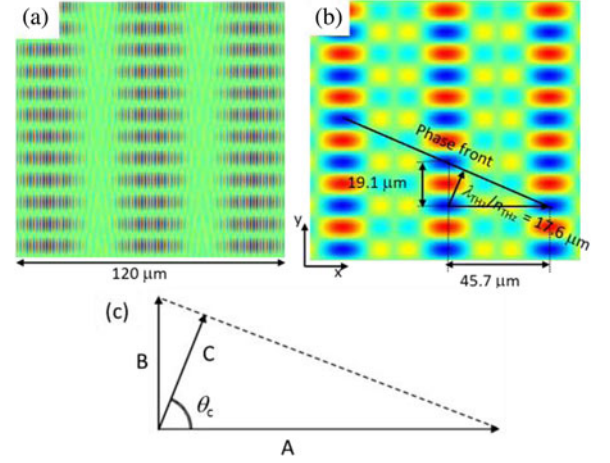


Fig. 4. Normalized electric-field distribution of (a) combined dual-wavelength pump beams within a finite angle and (b) excited second-order nonlinear polarization of the difference frequency. Here, $\lambda_1 = 1300$ nm, $\lambda_2 = 1317$ nm, the difference frequency = 3 THz, and the beam angle = 3.7° . (c) The geometric relation of A , B , and C , corresponding to the excited nonlinear polarization for the x -direction, the interference period of the pump beams for the y -direction, and the THz wavelength in the crystal, respectively.

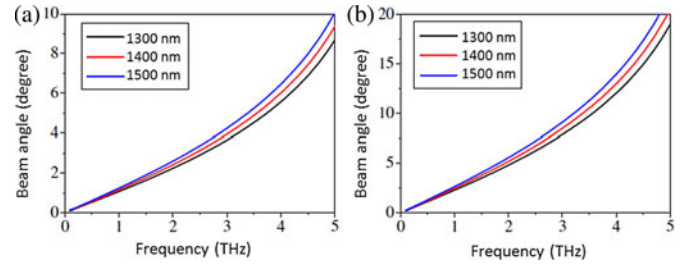


Fig. 5. Tuning angle (a) inside the crystal and (b) external to the crystal under 1300-, 1400-, and 1500-nm pump wavelengths, λ_1 .

The generated THz waves are directed along the propagation direction, just like a surf rider on nonlinear polarization waves, as shown in Fig. 4(b). Fig. 5 shows the required angle of the pump wavelength for frequency tuning inside the crystal [see Fig. 5(a)] and external to the crystal [see Fig. 5(b)]. The phase-matching condition is satisfied by changing the angle α for the required THz-wave and pump wavelengths. A slightly narrow tunability (~ 300 GHz for 3-THz-wave generation) was obtained at a fixed angle of $\alpha = 4.0^\circ$.

Fig. 6 shows the schematic of the experimental setup. The pump source for the DFG process, also used in our previous work [31], had a tunable range of 1250–1500 nm, 15 ns of pulse duration, and 0.88 mJ of pulse energy. The dual wavelength beams from the KTP OPO was focused by a spherical lens ($f = 500$ mm) before being separated by a half-beam splitter and then combined again within a finite angle. The spot diameter of the combined beam was 0.45 mm. The MgO:LiNbO₃ crystal used in this experiment was cut from a $5 \times 65 \times 6$ -mm wafer, and the x -surfaces at both ends were mirror polished. An array of seven Si-prism couplers was placed on the y -surface of the MgO:LiNbO₃ crystal.

To minimize the coupling gap between the crystal surface and the prism base, the y -surface of LN was also mirror polished.

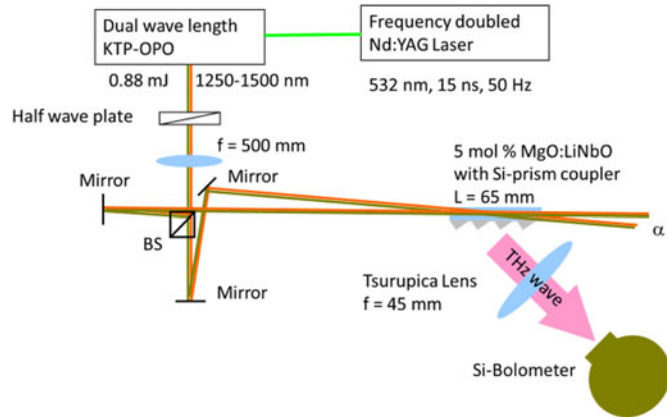


Fig. 6. Schematic of the experimental setup for Cherenkov phase-matching THz-wave generation with surfing configuration.

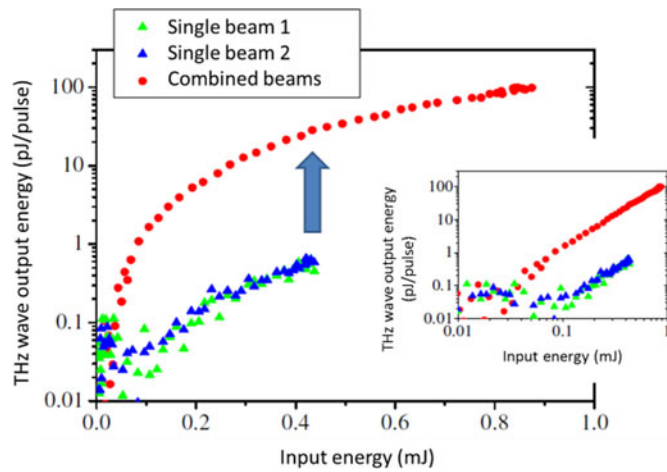


Fig. 7. Input-output properties of the THz wave for 1.0 THz generation with $\alpha = 2.49^\circ$. The circles and triangles denote the THz-wave output signal for the combined beams and single beams, respectively. The inset shows a double logarithmic plot of the input-output properties.

This polished surface prevented scattering of the pump beam, which generates free carriers at the Si-prism base.

The THz waves and polarizations of the pump were both parallel to the z -axis of the crystal. The THz-wave output was measured with a fixed 4-K Si bolometer.

The input-output properties of 1.0-THz-wave generation for $\alpha = 2.49^\circ$ as a function of pump energy are shown in Fig. 7. The triangles and circles denote the THz-wave output energy with individual single beams and with combined beams, respectively. Single-beam excitation was produced by interception of the other beam before entrance to the crystal. Maximum pump energy of only 0.44 mJ was used with single-beam pumping because half of the pump energy was dumped before entering the crystal (Fig. 6). The vertical axis in Fig. 7 represents the THz-wave pulse energy calculated from the output voltage of the Si-bolometer detector. A pulse energy of ~ 101 pJ pulse $^{-1}$ corresponded to a Si-bolometer voltage output of 1 V when the repetition rate was less than 200 Hz. Fig. 7 shows the remarkable enhancement ($\sim 50\times$) of the THz-wave generation from the surfing configuration. The inset of Fig. 7 shows a double

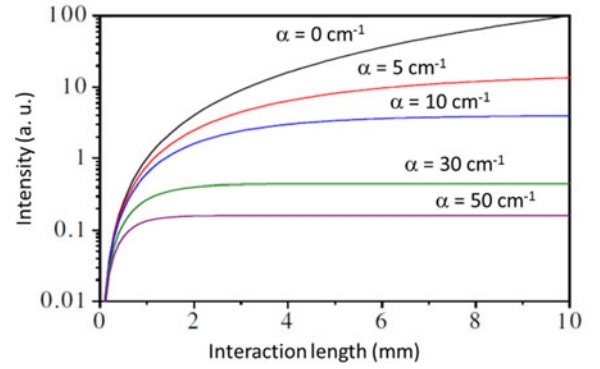


Fig. 8. Calculated intensity of overlapping in-phase THz waves in an absorptive media.

logarithmic plot of the input-output properties. The slope efficiencies under single-beam pumping and combined beams were almost the same. Thus, the enhancement factor of ~ 50 was a direct result of the suppression of the phase mismatch.

The generated THz waves at different positions in the crystal were in phase, and the output THz wave was enhanced. Fig. 8 shows the calculated intensity of the overlapping in-phase THz waves in the absorptive media. MgO:LiNbO $_3$ has an absorption coefficient of ~ 30 cm $^{-1}$ in the THz-frequency range [37]. The enhancement effect of the in-phase interference was effective for ~ 2 mm of travel distance for THz waves; this suggests an optimum pump-beam width in the y -axis direction of ~ 1.8 mm. In this study, the pump-beam width along the y -axis was ~ 0.45 mm, which resulted in a propagation length of 1.2 mm for the THz waves. Further, THz generation enhancement ($>50\times$) could be achieved by tightly focusing the beam along the z -axis only using a cylindrical lens.

The linewidth of the source was ~ 100 GHz, because each linewidth of a pump beam was ~ 60 GHz, as shown in our previous work [32]. This linewidth was slightly broader than that obtained from DAST crystal-based DFG [38] or injection-seeded THz parametric generation [7]. This occurred because the linewidth of the THz wave was depended on that of the pump source.

The confinement of the angle α to a 2.5° range made a broader tuning range. The beam-crossing point was set close to the surface of the crystal to generate THz waves, because LiNbO $_3$ has strong absorption for THz frequencies. In this configuration, the pump beam passing through the Si prism induced optical-carrier excitation in Si that prevented THz-wave transmission; the interaction length decreased at larger pumping angles.

D. Optimization of Pump-Beam Shape

A surface-emitting THz-wave source using DFG with a periodically poled LiNbO $_3$ (PPLN) crystal was developed to prevent absorption problems [39]–[44]. A surface-emitting THz wave radiated from the surface of the PPLN and propagated perpendicular to the pump-beam direction. The absorption and Fresnel losses were minimized because the THz wave was generated from the PPLN surface. Moreover, the phase-matching condition was met using a PPLN with an appropriate grating

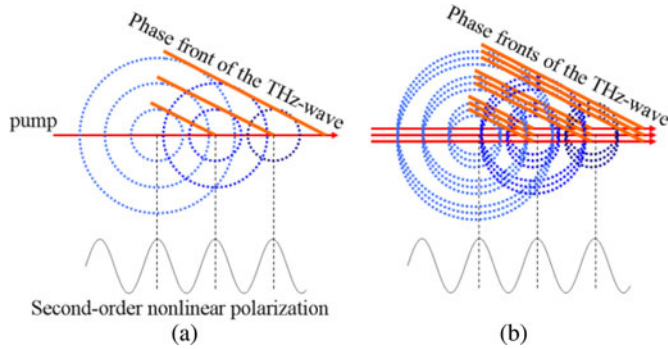


Fig. 9. (a) Ideal Cherenkov-type phase-matching condition. (b) Cherenkov-type phase-matching condition when the beam diameter of the exciting light is considered. In (b), the phase mismatch is caused by the finite size of the beam diameter.

period. Unfortunately, the tuning range of the resulting THz wave was limited by the design of the PPLN. Each PPLN had a tuning range of ~ 100 GHz; a wider tuning range was not realized with the quasi-phase-matching method [45].

We obtained efficient energy conversion in the low-frequency region below 0.5 THz and achieved a flat tuning spectrum by varying the pump wavelength during THz-wave tuning. The highest observed THz-wave energy was ~ 80 pJ pulse $^{-1}$, which was obtained over the broad spectral range of 0.2–2.0 THz. However, above 2 THz, it was difficult to obtain high conversion efficiency. In fact, the output decreased to almost zero at 3 THz. The decrease in the THz-wave output was attributed to the phase mismatch incurred by the finite size of the pump-beam diameter. As shown in Fig. 9(b), Cherenkov-type phase matching arises due to the superposition of spherical THz waves from the nonlinear polarization maxima created by the pump beams of two different frequencies in the NLO crystal. Thus, when the finite beam size is taken into account, the phase shift of the wave depends on the distance from the y -surface of the crystal. THz waves generated far from the crystal surface destructively interfere with those generated in the neighborhood of the crystal surface [33]. From our previous work, the beam diameter of the pump wave in the LiNbO₃ crystal was ~ 300 μ m, corresponding to a THz wavelength of 0.2 THz, and ten cycles of 2.0-THz waves (for LiNbO₃ with a refractive index of ~ 5.2). Because the 300- μ m beam diameter is over $15\times$ the wavelength of a THz wave above the 3-THz region, a phase mismatch occurred, and the THz-wave output decreased. In this experiment, we attempted to improve the THz-wave generation efficiency above 3 THz by optimizing the beam shape of the pump wave to decrease the beam-diameter dependence effect.

We demonstrated DFG using the experimental setup shown in Fig. 2. A dual-wavelength KTP OPO with a pulse duration of 15 ns, a pulse energy of 1.6 mJ, a 50-Hz repetition rate, and a tunable range of 1300–1600 nm was used for the DFG pumping source. The size of the MgO:LiNbO₃ crystal was $5 \times 65 \times 6$ mm. Both ends of the crystal's x -surface were optically polished, and an array of Si-prism couplers was placed on the y -surface of the crystal. The y -surface of the crystal was also optically polished. We used cylindrical lenses to reduce the pump-beam diameter.

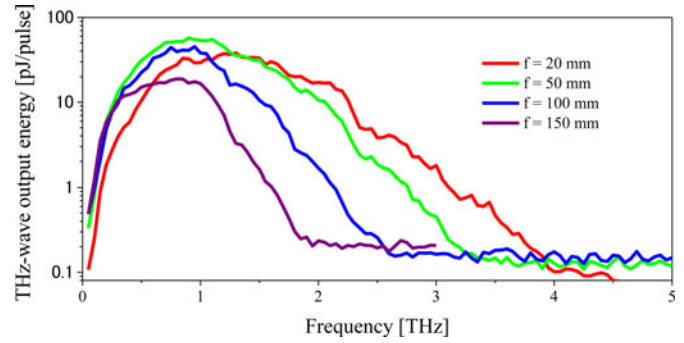


Fig. 10. THz-wave output spectra obtained using various cylindrical lenses, as measured by selecting the excitation wavelength at which the maximum output was obtained for each THz-wave frequency.

The focal lengths of the cylindrical lenses were 20, 50, 100, and 150 mm, and the beamwidths parallel to the crystal's y -axis were 35, 46, 83, and 127 μ m (full-width half-maximum), respectively. The pump power was adjusted, and the power density at the focus position was held constant at 200 MW cm $^{-2}$ for each lens.

The obtained THz-wave output spectrum is shown in Fig. 10. The vertical axis represents the THz-wave pulse energy calculated from the output voltage of a Si-bolometer detector. The horizontal axis represents the THz-wave frequency. A pulse energy of ~ 10 pJ pulse $^{-1}$ corresponded to a Si-bolometer voltage output of 1 V when the repetition rate was less than 200 Hz. The THz-wave output spectra were measured by selecting the excitation wavelength in which the maximum output was obtained for each THz-wave frequency. The output in the high-frequency region increased as the focal length of the cylindrical lens decreased. THz-wave generation was confirmed over the 3-THz region with 20- and 50-mm cylindrical lenses. The tunable range for the 20-mm cylindrical lens was ~ 0.2 –4.0 THz. This was the widest tuning range observed to date compared with our previous experiments on LiNbO₃ crystal-generated THz-wave sources. The pump-wave beam diameter in the LiNbO₃ crystal using the 20-mm cylindrical lens was ~ 35 μ m, which corresponded to 1.8-THz wave cycles at 3 THz. The phase mismatch is thought to have decreased as the beam diameter decreased, leading to an improvement in the output in the high-frequency region. The conversion efficiency decreased because the pump-beam diameter corresponded to more than 2.3-THz wave cycles, and the absorption coefficient increased rapidly above 4 THz. The absorption coefficient of the crystal at 4 THz was 425 cm $^{-1}$ [46]. When the pump beam moved 100 μ m away from the y -surface of the crystal, 98.6% of the output was lost. Narrowing the beam diameter further was difficult due to diffraction. As the beam diameter narrowed, the confocal length shortened, and the conversion efficiency decreased. The low-frequency-region generation efficiency was expected to decrease for the 20-mm cylindrical lens case because the confocal length shortened. This problem was prevented by using a waveguide structure [34]. By limiting the beam diameter of the pump wave to half the wavelength using only the waveguide mode for THz-wave generation, the phase mismatch was neglected

and the absorption loss reduced. This is because the distance from the y -surface to the pump beam dropped to almost zero, resulting in higher conversion efficiency and a wider spectrum.

E. Prism-Coupled Cherenkov Phase-Matched THz-Wave Generation Using a DAST Crystal

Cherenkov THz radiation is generated inside a nonlinear crystal when the velocity of the polarization excited by DFG is greater than the phase velocity of the radiated wave. In terms of the dispersion of the refractive index of most nonlinear crystals, the refractive index at the THz region is higher than that at optical frequencies. This may result in behavior that satisfies (1). The Cherenkov angle θ_{crystal} depends strongly on the NLO crystal, because the refractive index at the THz frequency and that at the optical frequency both determine the Cherenkov angle. The emitted THz radiation propagates at the Cherenkov angle to the crystal–air interface. THz generation is suppressed by the total internal reflection, when the angle is larger than the critical angle. To prevent this, we used a cladding material with a suitable refractive index formed into a prism. The angle θ_{clad} of the cladding–nonlinear-crystal interface is important for practical applications and can be determined using Snell's law as follows:

$$\begin{aligned} \theta_{\text{clad}} &= \frac{\pi}{2} - \beta = \frac{\pi}{2} - \arcsin\left(\frac{n_{\text{THz}}}{n_{\text{clad}}} \sin(\alpha)\right) \\ &= \frac{\pi}{2} - \arcsin\left(\frac{n_{\text{THz}}}{n_{\text{clad}}} \sin\left(\frac{\pi}{2} - \theta_{\text{crystal}}\right)\right) \\ &= \frac{\pi}{2} - \arcsin\left(\frac{n_{\text{THz}}}{n_{\text{clad}}} \sin\left(\frac{\pi}{2} - \arccos\left(\frac{n_1 \lambda_2 - n_2 \lambda_1}{n_{\text{THz}}(\lambda_2 - \lambda_1)}\right)\right)\right) \\ &= \arccos\left(\frac{n_1 \lambda_2 - n_2 \lambda_1}{n_{\text{clad}}(\lambda_2 - \lambda_1)}\right) \end{aligned} \quad (4)$$

where n_{clad} is the refractive index of the cladding layer in the THz-frequency range. This equation is equivalent to a model in which the THz wave radiates directly into the cladding layer. It indicates that n_{clad} should be larger than that for the nonlinear crystal at the pump frequency and also that it is not necessary to account for the refractive index of the crystal at THz frequencies (i.e., the equation does not depend on n_{THz}). We call this method prism-coupled Cherenkov phase matching (PCC-PM). The silicon is a proper material for Cherenkov radiation using nonlinear crystals, considering the PCC-PM THz-wave generation comparing the refractive index of the crystal at optical frequencies with that of silicon ($n_{\text{Si}} \sim 3.4$ across the entire THz-frequency range).

The organic nonlinear crystal DAST was also an attractive material for THz generation [31], [47] because the crystal has a very large nonlinear coefficient. However, the strong absorption of the DAST crystal for THz waves prevents the efficient THz radiation. The PCC-PM method, however, allowed efficient THz generation with very high nonlinear efficiency. DAST has very similar refractive indices in the near-infrared and THz-frequency regions, suggesting its use for collinear phase matching. Fig. 11 shows the phase-matching vectors under the following conditions: $k_{\text{THz}} > k_1 - k_2$, $k_{\text{THz}} = k_1 - k_2$, and $k_{\text{THz}} < k_1 - k_2$.

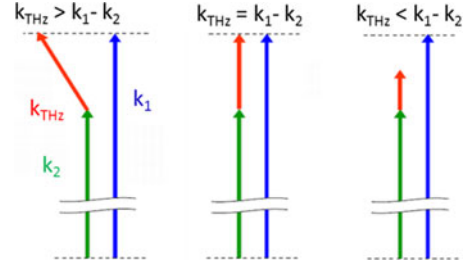


Fig. 11. Phase-matching vectors of the DFG process for three different relative wave vectors of the THz and optical radiation. The blue, green, and red arrows denote the pump, signal, and THz radiation, respectively. Cherenkov phase matching is achieved when $k_{\text{THz}} > k_1 - k_2$; collinear phase matching is achieved when $k_{\text{THz}} = k_1 - k_2$. Phase matching cannot be achieved when $k_{\text{THz}} < k_1 - k_2$.

$k_1 - k_2$. Perfect phase matching in a collinear configuration is satisfied when $k_{\text{THz}} = k_1 - k_2$. Cherenkov configuration is also satisfied when $k_{\text{THz}} > k_1 - k_2$. However, when $k_{\text{THz}} < k_1 - k_2$, phase matching cannot be achieved.

Although the Cherenkov phase-matching condition cannot be satisfied when $k_{\text{THz}} < k_1 - k_2$ in the bulk, the PCC-PM condition can be satisfied by applying a Si-cladding layer, as follows from (4). The Cherenkov angle inside the crystal strongly depended on the dispersion characteristics of the DAST crystal; this means that the pump wavelength influenced the angle. When the wavelength of a pump beam is 1300 nm, the Cherenkov phase-matching condition cannot be satisfied across the entire range of THz frequencies.

Fortunately, (4) tells us that the Cherenkov condition inside the crystal does not have to be satisfied for THz generation using the PCC-PM method. The THz radiation experiences the refractive index of the cladding material at the interface: therefore, it can be coupled out of the cladding layer regardless of the relative refractive indices within the nonlinear crystal. The calculated angles inside the crystal ranged from 0° to 40° , and the THz radiation was totally reflected at the interface with air, as predicted from (4). If the Si cladding functions only as an output coupler, it follows that the Si coupler will not work as a Cherenkov phase-matching component, and the THz radiation at the frequency where the phase-matching condition is not satisfied cannot be out-coupled unless the Si cladding is formed into a prism.

We used a 100- μm -thick DAST single crystal in this experiment. The crystal was hexagonal, as illustrated in Fig. 12, so that we could achieve b -axis propagation of the two pump beams. A Si prism was coupled along the $(0 \ 0 \ 1)$ plane of the DAST crystal because the as-grown DAST had a very flat surface in this plane. We used a dual-wavelength KTP OPO with a tunable range of 1300–1600 nm, a pulse energy of 1.5 mJ, and a pulse duration of 15 ns as the pump, as in our previous work [20]–[23]. The polarizations of the two pumps were parallel to the a -axis of the DAST crystal, which had the highest nonlinear coefficient component; the THz radiation was generated parallel to the a -axis. The pump beam was focused to a 46- μm diameter beam using a cylindrical lens with a 50-mm focal length, resulting in a power density of $\sim 50 \text{ MW cm}^{-2}$. The emitted THz radiation

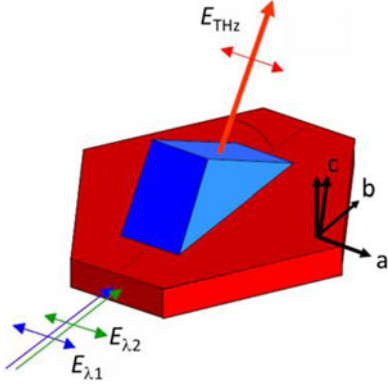


Fig. 12. Schematic diagram of the experimental configuration. The DAST single crystal is shown in red, and the Si-prism coupler is shown in blue.

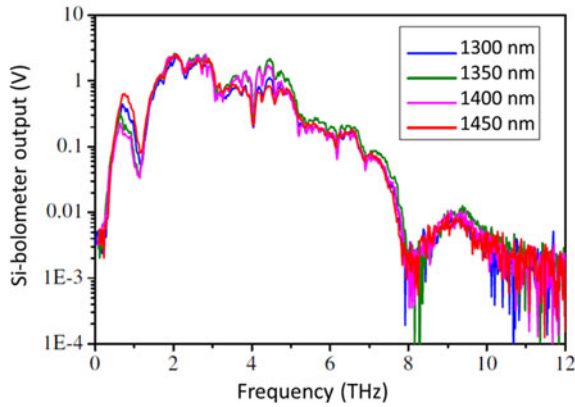


Fig. 13. THz output spectra under pump wavelengths ranging from 1300 to 1450 nm.

was detected using a liquid-helium-cooled Si bolometer with an electrical gain of 1000.

Fig. 13 shows the collected THz output spectra under different pump wavelengths. THz radiation was generated at levels of less than 1 THz to more than 10 THz, with spectra that were almost independent of the pump wavelength. The dip at 8 THz originated from the transmission character of a filter inside the Si bolometer. When collinear phase matching is used to generate THz radiation, a deep dip in the spectra is observed at ~ 1.1 THz [31], [48]. This is suppressed here because the Cherenkov method resulted in surface emission. We successfully obtained ~ 100 times higher signal-to-noise ratio. Additionally, radiation was generated below 1 THz, which cannot be generated using collinear phase matching with 1300–1450-nm pumping [49]. At frequencies above ~ 10 THz, the detection efficiency of the bolometer decreased; this explains the low observed power at higher frequencies. However, the collected power extended to higher frequencies than that observed when using bulk LiNbO₃ in our previous work [21]. Although THz radiation generated far from the crystal-cladding interface interfered with that generated near the interface resulting in destructive interference, the radiation generated deep within the crystal was attenuated due to the large absorption coefficient of the crystal. The absorption coefficient of the DAST crystal in the

2–10 THz range was $100\text{--}200\text{ cm}^{-1}$. THz wave output energy that propagated the distance determined by the beam diameter ($\sim 50\text{ }\mu\text{m}$) was attenuated by 30–60%. The output voltage of the Si bolometer was converted to energy by considering that $1\text{ V} \approx 20\text{ pJ pulse}^{-1}$ for low-repetition-rate detection and that we had a gain of 1000 at the bolometer. The highest-energy THz pulse obtained was $\sim 50\text{ pJ}$ (3.3 mW at peak). The obtained output energy was higher than that obtained by collinear phase matching using a DAST crystal under almost the same power density [31], [48].

We demonstrated PCC-PM THz generation using a DAST crystal. The spectra were broadband and almost independent of the pump wavelength over a 1300–1450 nm range. The PCC-PM method had the advantage of suppressing the strong absorption in the nonlinear crystal. The conversion efficiency using collinear and noncollinear phase-matching methods is inversely proportional to the square of the absorption coefficient. The large nonlinearity in the crystal cannot be fully exploited due to the large absorbance. Organic nonlinear crystals, however, can be used effectively with this method because the surface emission is not influenced by absorption in the crystal. Hebling *et al.* described a figure of merit for several nonlinear crystals [50] in terms of their nonlinearity and absorption. GaSe had the highest figure of merit; however, DAST had larger optical nonlinearity. Using the surface-emission method described here, the absorption coefficient ceased to be an issue, suggesting that DAST may be a more efficient material for generating THz radiation using DFG. The method described here also has the advantage of relaxing the phase-matching requirement. Although nonlinear crystals need to satisfy the requirement of phase-matching condition (such as quasi-phase matching, noncollinear phase matching, or birefringence), this condition is much less stringent for the PCC-PM. Furthermore, the method does not require a specific pump wavelength. Thus, PCC-PM could allow the realization of simple, compact, highly efficient, ultrabroadband THz sources using a variety of nonlinear crystals.

III. THz GENERATION FROM WAVEGUIDE STRUCTURE

A. THz-Wave Generation From a LiNbO₃ Crystal Slab-Waveguide Structure

As mentioned previously, THz radiation generated far from the crystal surface interfered with that generated near the surface, resulting in destructive interference. Reducing the beam diameter in the propagation direction within the crystal to approximately one-half the wavelength removed the phase-matching limitation in that direction. However, tight focusing of the beam diameter also reduced the interaction length, decreasing the output power. In this section, Cherenkov-radiated THz radiation is described in which an MgO-doped LiNbO₃ slab waveguide $3.8\text{ }\mu\text{m}$ thick was used. The waveguide structure resulted in a reduction in beam diameter in the propagation direction, which removed the phase mismatch while retaining a long interaction length.

Fig. 14 shows the relation between the Cherenkov angle and the critical angle of several cladding materials. Because diamond, polyethylene, Ge, and Si have low dispersion and low

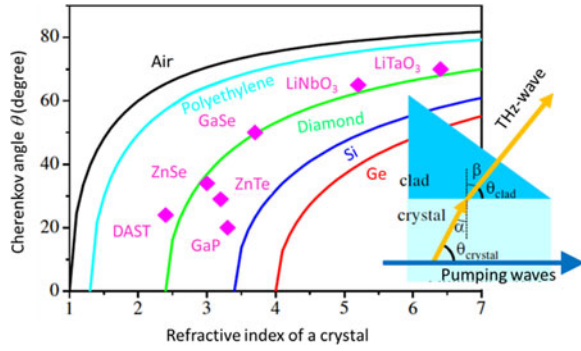


Fig. 14. Cherenkov angle for various nonlinear crystals (pink-colored diamonds) and calculated critical angle between the crystal and the cladding. The black, aqua, green, blue, and red curves represent air, polyethylene, diamond, Si, and Ge as cladding materials, respectively. Total internal reflection occurs below the curve. The inset shows a schematic of the Cherenkov radiation and output coupling of the THz-frequency wave.

absorbance character for THz frequencies, we chose these materials as cladding materials. Total internal reflection occurs below the curve in Fig. 14. For example, LiNbO_3 has a refractive index of 2.2 and 5.2 at near-infrared and THz-wave frequencies, respectively, resulting in a 65° Cherenkov angle in the crystal. The critical angle of the total internal reflection from the crystal to Ge, Si, diamond, polyethylene, and air are 40° , 49° , 63° , 76° , and 79° , respectively. The figure suggests that diamond, Si, and Ge prevent total internal reflection of the Cherenkov radiation for the LiNbO_3 crystal.

We used silicon and $\text{MgO}:\text{LiNbO}_3$ as the cladding material and nonlinear crystal, respectively, because the silicon is an appropriate Cherenkov-radiation output coupler for many crystals as mentioned previously. Widely tunable monochromatic THz waves were generated in the frequency range 0.2–4.0 THz, although the nonlinear crystal was bulk LiNbO_3 . The highest THz-wave energy was $\sim 80 \text{ pJ pulse}^{-1}$; this energy was obtained over a broad spectral region of 1.0–2.0 THz. Although the generated waves were widely tunable, the THz-wave-generation conversion efficiency at higher frequencies (above 2.0 THz) was slightly low. This was caused by a phase mismatch in the generated THz waves in the direction of propagation [21]. In our previous study, the pump-wave beam diameter in the LiNbO_3 crystal was in the range of 35–127 μm . For a 35- μm pump-beam diameter, the beamwidth corresponded to ~ 2.4 cycles of 4.0-THz waves because the refractive index of LiNbO_3 is ~ 5.2 . THz-frequency waves generated far from the crystal surface interfered with those generated in the neighborhood of the crystal surface, resulting in destructive interference. Reducing the beamwidth diameter in the crystal in the direction of THz-wave propagation to close to one-half the THz wavelength, i.e., $\sim 20 \mu\text{m}$, removed the phase-mismatch effect in that direction.

We prepared a slab waveguide using a LiNbO_3 crystal. A Y-cut $\text{MgO}:\text{LiNbO}_3$ on a thick congruent LiNbO_3 substrate was polished down to 3.8 μm . Because the refractive indices of congruent LiNbO_3 and $\text{MgO}:\text{LiNbO}_3$ were 2.15 and 2.22 at 1300 nm, the thin layer of $\text{MgO}:\text{LiNbO}_3$ worked as an optical slab waveguide [51]. The waveguide device was 70 mm long (in the x -axis direction) and 5 mm wide. Each X-surface facet was

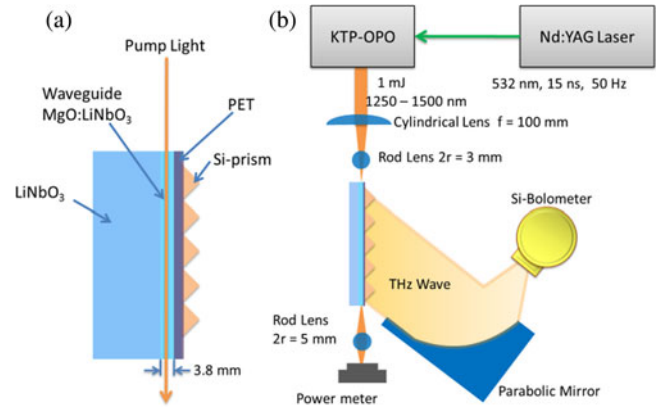


Fig. 15. (a) Schematic of the LiNbO_3 waveguide device with a Si-prism array coupler. (b) THz-wave detection experimental setup.

mechanically polished to obtain an optical surface. Fig. 15(b) shows the experimental setup for the DFG demonstrated in this section. A dual-wavelength KTP OPO with a pulse duration of 15 ns, a pulse energy of 1 mJ, and a tunable range of 1300–1600 nm was used as the pump source, as in previous sections. A thin (3.4 μm thick) polyethylene terephthalate (PET) film was placed between the array of Si-prism couplers and the Y-surface of the $\text{MgO}:\text{LiNbO}_3$. Directly placing an array of Si-prism couplers on the Y-surface of the $\text{MgO}:\text{LiNbO}_3$ inhibits the function of the $\text{MgO}:\text{LiNbO}_3$ layer as a waveguide for pump waves because the refractive index of Si in the near-infrared region is higher (~ 3.5) than that of LiNbO_3 (~ 2.2). PET, in contrast, has a lower refractive index in that region (~ 1.3); thus, adding a thin PET film does not inhibit the waveguide function of the crystal. An array of Si-prism couplers on a PET film worked as a coupler for THz-frequency waves because the PET film is thin compared with the wavelength of the THz-frequency waves. Fig. 15(a) shows schematic of the THz-wave emitting system and the coupling system of the pump wave. To couple the pump waves, the pump beam was reduced to a few micrometers in the x -axis direction by a 3-mm diameter glass rod lens. The width of the pump beams in the z -direction was $\sim 1.9 \text{ mm}$. The waveguide power density was $\sim 53 \text{ MW cm}^{-2}$, estimated from the pump-wave pulse energy after waveguide propagation ($\sim 60 \mu\text{J}$). We did not observe or calculate the waveguide mode of the structure in which a thin $\text{MgO}:\text{LiNbO}_3$ layer was sandwiched by a thick congruent LiNbO_3 layer and a thin PET film. This remains an area of future work to optimize the waveguide structure. The pump wave and THz-frequency wave polarizations were parallel to the crystal's z -axis. The THz-wave output was measured with a fixed 4-K Si bolometer.

Fig. 16 shows a THz-wave spectrum at various wavelengths, λ_1 , from 1250 to 1400 nm. The spectrum was obtained by varying λ_2 for a fixed λ_1 . The figure certainly shows a high-frequency THz radiation approaching 7.2 THz. Since the longitudinal-optical (LO) phonon mode has the strong absorption at 7.5 THz, the THz-wave generation near 7.2 THz was not observed. The THz-wave spectrum did not depend on the pump wavelength because the near-infrared refractive index was almost constant over the 1250–1450 nm range. The inset of

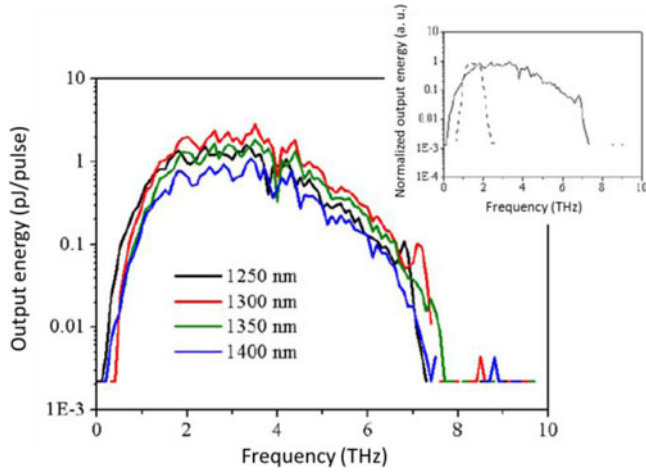


Fig. 16. THz-frequency spectra of waveguided-Cherenkov radiation. The black, red, blue, and green curves represent λ_1 pumping wavelengths of 1250, 1300, 1350, and 1400 nm, respectively. The inset shows a comparison of the normalized tuning spectrum of the waveguided-Cherenkov radiation source under 1250-nm pumping (solid curve) and the spectrum from a THz parametric generator (TPG) (dashed curve).

Fig. 16 shows a comparison of the normalized tuning spectrum of the waveguided Cherenkov radiation source and the injection-seeded THz parametric generator (TPG) [7]. Each THz source was based on the same nonlinear crystal, MgO:LiNbO₃. Using the waveguide structure, THz generation from Cherenkov radiation has the extremely wide tuning-frequency range compared with that from the TPG. We converted the output voltage of the Si bolometer to the actual THz-wave energy, given that 1 V \approx 20 pJ pulse⁻¹ for low-repetition rate detection, pulsed heating of the Si device, and an amplifier gain of 1000 at the bolometer. The highest THz-wave energy obtained was \sim 3.2 pJ, and the energy conversion efficiency from the λ_1 wave (30 μ J pulse⁻¹) was \sim 10⁻⁵%. This value is comparable to our previous work on Cherenkov radiation using the bulk crystal, despite the low excitation energy of only 30 μ J. To our knowledge, the tuning range of THz-wave generation obtained in this study using LiNbO₃ is the largest to date.

The THz-wave emitting angle was absolutely constant, as the Si dispersion in this range was almost flat. The device would work well in an optical rectification process using a femtosecond laser [52]. A range of 0.1–7.2 THz, free from structural dips, is suitable for ultrashort pulse generation. Also, the surface emission process used here is lossless, permitting the generation of a continuous, widely tunable THz-frequency range [41]. The compact and robust THz-wave sources realized by this method only require the use of two commercially available diode lasers. Although we demonstrated THz generation using only a LiNbO₃ crystal, the approach described in this study can easily be adopted for other nonlinear crystals such as DAST, ZGP, ZnTe, ZnSe, GaP, GaSe, and LiTaO₃. By choosing the best cladding materials for the nonlinear crystals (in many cases, Si or Ge), the Cherenkov condition was satisfied, and control over the crystal angles to satisfy phase-matching conditions, such as birefringence phase-matching, was not required. This method

opens the door to simple, compact, highly efficient ultrabroadband THz-wave sources.

B. THz-Wave Generation From a LiNbO₃ Crystal Using a Ridge-Type Waveguide Structure

One of the most powerful tools for THz imaging is time-domain spectroscopy (TDS). Opaque samples having either high water content or metal backing can be measured with reflection-type THz TDS, which can be used not only for spectroscopy but also for tomographic imaging [53], [54]. Because the electromagnetic field of the subpicosecond THz pulses is measured directly with THz TDS, the multilayered structure of a sample is imaged by detecting the echo pulses reflected from each layer. This technique is valuable in industry because the unique transmission characteristics of the THz waves enable the inspection of multilayered paints in industrial products or tablet coatings [55], [56], which are not measurable with optical coherence tomography (OCT) [57].

As is restricted by the temporal duration of the THz pulses used, the conventional axial resolution of THz tomography remains a few tens of microns. The common \sim 10- μ m thickness of the coatings in various industrial products and the stratum corneum of human skin require a higher depth resolution. In terms of tomographic imaging, generation of short and broadband THz pulses improves the depth resolution. We have developed an all-fiber laser system that produces 17-fs optical pulses at a wavelength of 1.56 μ m and have generated and detected broadband THz pulses ranging from 0.1 to 27.0 THz using a DAST crystal. The temporal waveform of the generated THz pulses has multiple peaks [58].

We used a MgO:LiNbO₃ ridge-type waveguide (width 5.2 μ m; thickness 3.8 μ m; length 10 mm) in this section. The crystal was coupled to a spherical Si prism, which satisfied the PCC-PM condition, as shown in Fig. 17. When the waveguide crystal was illuminated by the incoming pump beam, THz radiation was generated due to optical rectification. The THz radiation emanated as spherical waves from each point of the waveguide and was enhanced 50° from the pump-beam axis (Fig. 17). Based on the PCC-PM method, a Si prism was used to cancel the total internal reflection and bring out the generated THz waves [24], [25]. The incident beam entering the waveguide was monitored by an infrared vidicon camera (C2741, Hamamatsu Photonics).

The experimental setup using the ridge-type waveguide is shown in Fig. 18. The average power, pulse width, and repetition frequency of the pump femtosecond fiber laser were 50 mW, 17 fs, and 48 MHz, respectively. The optical pulses were divided into two beams for THz-wave generation and detection. The THz waves radiated from a MgO:LiNbO₃ plate ($t = 3.8 \mu$ m). The pump beam was tightly focused as close to the THz exit surface as possible using an aspherical lens with a focal length of 4.5 mm. The pump diameter before the aspherical lens was 1.2 mm (FWHM). To avoid leakage of a pump beam into the Si prism, MgO:LiNbO₃ and Si sandwich a thin PET film. Using configuration of parabolic mirrors, LT-GaAs PCA detect generated THz pulses. The temporal waveform of the THz waves

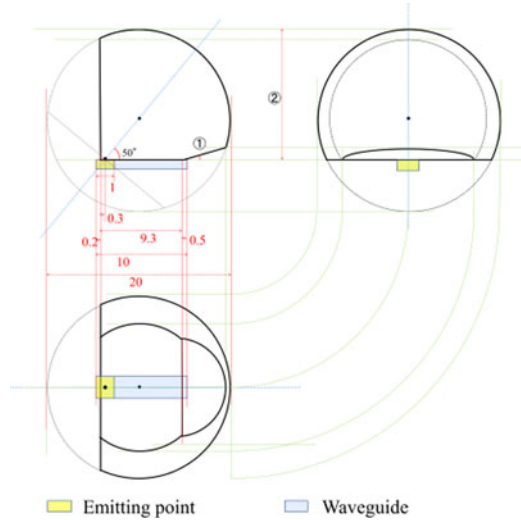


Fig. 17. Schematic illustration of a prism-coupled ridge-type waveguide. The angle between the pump beam and the enhanced radiation satisfying the Cherenkov phase-matching condition is calculated to be 50° .

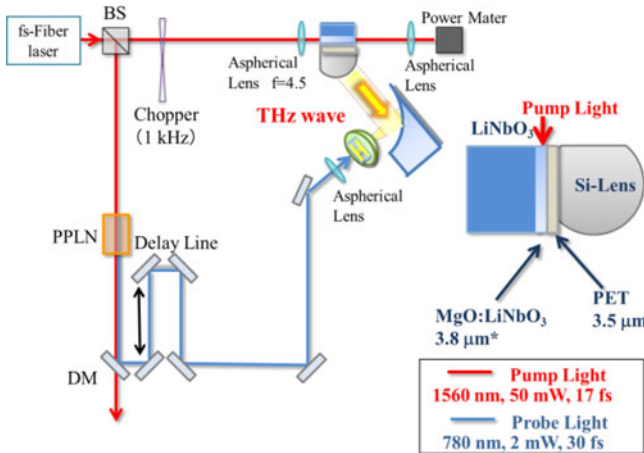


Fig. 18. Experimental setup for THz generation from a LiNbO_3 waveguide pumped by a femtosecond laser.

was traced by scanning a delay stage, whereby SHG pulses generated with a PPLN were used as the probe pulses. The signal obtained was then fed into a preamplifier and detected with a lock-in amplifier.

The THz waveform radiated from the waveguide illuminated by a 1560-nm pump pulse is shown in Fig. 19(a). The shape of the obtained THz pulse is an ideal half-cycle, with a pulse width of 193 fs. Fig. 19(b) shows the corresponding spectrum obtained by Fourier transformation of the time-domain spectrum. The bandwidth of the spectrum was ~ 4 THz. The attenuation of the THz waves due to the large absorption of the LiNbO_3 crystal was suppressed because the waveguide form shortens the propagation length. Here, the absorption coefficient of the LiNbO_3 crystal at 4 THz was 425 cm^{-1} [46]; the bandwidth of the generated THz waves from the bulk LiNbO_3 crystal illuminated by femtosecond laser pulses was quite narrow [13], thus reducing the absorption. However, the correct bandwidth of the spectrum must be wider than that obtained in terms of the pulse width of

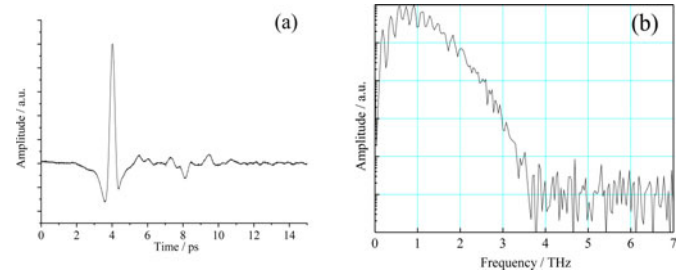


Fig. 19. (a) Temporal waveform of the detected THz pulse. (b) Corresponding spectrum obtained by the Fourier transformation of the temporal waveform.

the time-domain spectrum. Improvements in the performance of this method require more work in this area.

Because tomographic imaging requires multiple reflections of the THz pulses, a half-cycle THz pulse is necessary to suppress the interference of waves reflected from each layer. Thus, a smaller pulse width is required for higher depth resolution. The shape of the generated THz pulse is an ideal half-cycle, and the pulse width is 193 fs, which corresponds to the depth resolution of $29.0 \mu\text{m}$. Because this pulse width is sufficiently narrow compared with that of THz pulses generated from PCA, the THz-pulse generation using a waveguide crystal should be a good fit for tomographic imaging.

IV. CONCLUSION

We reviewed THz-wave generation based on the Cherenkov-type radiation using bulk and waveguide crystals. In Section II-B, we presented a Cherenkov phase-matching method for monochromatic THz-wave generation using the DFG process with a LiNbO_3 crystal, which resulted in both high conversion efficiency and wide tunability. Section II-C presented Cherenkov phase matching with a “surfing” configuration for the bulk crystal. Efficient THz-wave generation and a high enhancement factor were obtained. Section II-D presented improvement of the THz-wave generation efficiency above 3 THz by shaping the pump beam with a cylindrical lens. Reducing the beam diameter allowed the generation of monochromatic THz waves with wide tunability over the 0.2–4.0 THz range. In Section II-E, we presented the PCC-PM method, in which a prism with a suitable refractive index at THz frequencies was coupled to the crystal. Using a DAST crystal, this method produced THz-wave radiation with wide tunability; no deep absorption features were evident, and the obtained spectra did not depend on the pump wavelength.

In Section III-A, using a slab-type MgO:LiNbO_3 waveguide, we successfully widened the tuning range of the monochromatic THz-wave source using Cherenkov radiation based on DFG. The range obtained was extremely wide, from 0.1 to 7.2 THz, and exhibited no structural dips in the tuning range. In Section III-B, we presented Cherenkov-type THz generation using a ridge-type waveguide under the PCC-PM condition, pumped by a femtosecond fiber laser. THz-wave radiation with a wide frequency range and ideal temporal half-cycle pulse, suitable for reflection tomography imaging, was realized.

ACKNOWLEDGMENT

The authors thank Dr. T. Shibuya, Dr. H. Minamide, and H. Ito of RIKEN; Y. Avetisyan of the Microwave Engineering Department, Yerevan State University; K. Kajiki of Canon; and Dr. S. Fan and H. Takeuchi of the Department of Electrical Engineering, Nagoya University, for their experimental support for the part of the work.

REFERENCES

- [1] M. Tonouchi, "Cutting-edge terahertz technology," *Nat. Photon.*, vol. 1, pp. 97–105, Feb. 2007.
- [2] B. Ferguson and X.-C. Zhang, "Materials for terahertz science and technology," *Nat. Mater.*, vol. 1, no. 1, pp. 26–33, Sep. 2002.
- [3] J. M. Yarbrough, S. S. Sussman, H. E. Puthoff, R. H. Pantell, and B. C. Johnson, "Efficient, tunable optical emission from LiNbO_3 without a resonator," *Appl. Phys. Lett.*, vol. 15, no. 5, pp. 102–105, Aug. 1969.
- [4] B. C. Johnson, H. E. Puthoff, J. SooHoo, and S. S. Sussman, "Power and linewidth of tunable stimulated far-infrared emission in LiNbO_3 ," *Appl. Phys. Lett.*, vol. 18, no. 5, pp. 181–183, Mar. 1971.
- [5] M. A. Piestrup, R. N. Fleming, and R. H. Pantell, "Continuously tunable submillimeter wave source," *Appl. Phys. Lett.*, vol. 26, no. 8, pp. 418–421, Apr. 1975.
- [6] K. Kawase, M. Sato, T. Taniuchi, and H. Ito, "Coherent tunable THz-wave generation from LiNbO_3 with monolithic grating coupler," *Appl. Phys. Lett.*, vol. 68, no. 18, pp. 2483–2485, Apr. 1996.
- [7] K. Kawase, H. Minamide, K. Imai, J. Shikata, and H. Ito, "Injection-seeded terahertz-wave parametric generator with wide tunability," *Appl. Phys. Lett.*, vol. 80, no. 2, pp. 195–197, Jan. 2002.
- [8] G. D. Boyd, T. J. Bridges, C. K. N. Patel, and E. Buehler, "Phase matched submillimeter wave generation by difference-frequency mixing in ZnGeP_2 ," *Appl. Phys. Lett.*, vol. 21, no. 11, pp. 553–555, Dec. 1972.
- [9] W. Shi, Y. J. Ding, N. Fernelius, and K. Vodopyanov, "Efficient, tunable, and coherent 0.18–5.27-THz source based on GaSe crystal," *Opt. Lett.*, vol. 27, no. 16, pp. 1454–1456, Aug. 2002.
- [10] T. Tanabe, K. Suto, J. Nishizawa, K. Saito, and T. Kimura, "Tunable terahertz wave generation in the 3- to 7-THz region from GaP," *Appl. Phys. Lett.*, vol. 83, pp. 237–239, Jul. 2003.
- [11] K. Kawase, M. Mizuno, S. Sohma, H. Takahashi, T. Taniuchi, Y. Urata, S. Wada, H. Tashiro, and H. Ito, "Difference-frequency terahertz-wave generation from DAST by use of an electronically tuned Ti: Sapphire laser," *Opt. Lett.*, vol. 24, pp. 1065–1067, Aug. 1999.
- [12] D. H. Auston, "Subpicosecond electro-optic shock waves," *Appl. Phys. Lett.*, vol. 43, pp. 713–715, Oct. 1983.
- [13] L. Xu, X.-C. Zhang, and D. H. Auston, "Terahertz beam generation by femtosecond optical pulses in electro-optic materials," *Appl. Phys. Lett.*, vol. 61, pp. 1784–1786, Oct. 1992.
- [14] M. Nagai, E. Matsubara, and M. Ashida, "High-efficiency terahertz pulse generation via optical rectification by suppressing stimulated Raman scattering process," *Opt. Exp.*, vol. 20, pp. 6509–6514, Mar. 2012.
- [15] C. P. Hauri, C. Ruchert, C. Vicario, and F. Ardana, "Strong-field single-cycle THz pulses generated in an organic crystal," *Appl. Phys. Lett.*, vol. 99, pp. 161116.1–161116.3, Oct. 2011.
- [16] J. A. Fülöp, L. Pálfalvi, S. Klingebiel, G. Almási, F. Krausz, S. Karsch, and J. Hebling, "Generation of sub-mJ terahertz pulses by optical rectification," *Opt. Lett.*, vol. 37, pp. 557–559, Feb. 2012.
- [17] K. H. Yang, P. L. Richards, and Y. R. Shen, "Coherent phonon generation by optical mixing in a one-dimensional superlattice," *J. Appl. Phys.*, vol. 44, pp. 1417–1419, Apr. 1973.
- [18] T. Dekorsy, H. Auer, C. Waschke, H. J. Bakker, H. G. Roskos, H. Kurz, V. Wagner, and P. Grosse, "Emission of submillimeter electromagnetic waves by coherent phonons," *Phys. Rev. Lett.*, vol. 74, pp. 738–741, Jan. 1995.
- [19] K. Takeya, Y. Takemoto, I. Kawayama, H. Murakami, T. Matsukawa, M. Yoshimura, Y. Mori, and M. Tonouchi, "Terahertz emission from coherent phonons in lithium ternary chalcopyrite crystals illuminated by 1560 nm femtosecond laser pulses," *Europhys. Lett.*, vol. 91, pp. 20004-p1–p4, Jul. 2010.
- [20] K. Suizu, T. Shibuya, T. Akiba, T. Tutui, C. Otani, and K. Kawase, "Cherenkov phase-matched monochromatic THz-wave generation using difference frequency generation with lithium niobate crystal," *Opt. Exp.*, vol. 16, pp. 7493–7498, May 2008.
- [21] T. Shibuya, T. Tsutsui, K. Suizu, T. Akiba, and K. Kawase, "Efficient Cherenkov-type phase-matched widely tunable THz-wave generation via an optimized pump beam shape," *Appl. Phys. Exp.*, vol. 2, pp. 032302-1–3, Feb. 2009.
- [22] K. Suizu, K. Koketsu, T. Shibuya, T. Tsutsui, T. Akiba, and K. Kawase, "Extremely frequency-widened terahertz wave generation using Cherenkov-type radiation," *Opt. Exp.*, vol. 17, pp. 6676–6681, Apr. 2009.
- [23] K. Suizu, T. Tsutsui, T. Shibuya, T. Akiba, and K. Kawase, "Cherenkov phase-matched THz-wave generation with surfing configuration for bulk lithium niobate crystal," *Opt. Exp.*, vol. 17, pp. 7102–7109, Apr. 2009.
- [24] K. Suizu, T. Shibuya, H. Uchida, and K. Kawase, "Prism-coupled Cherenkov phase-matched terahertz wave generation using a DAST crystal," *Opt. Exp.*, vol. 18, pp. 3338–3344, Feb. 2010.
- [25] K. Kawase, S. Ichino, K. Suizu, and T. Shibuya, "Half cycle terahertz pulse generation by prism-coupled Cherenkov phase-matching method," *J. Infrared Milli. Terahz. Waves*, vol. 32, pp. 1168–1177, May 2011.
- [26] D. H. Auston, K. P. Cheung, J. A. Valdmanis, and D. A. Kleinman, "Cherenkov radiation from femtosecond optical pulses in electro-optic media," *Phys. Rev. Lett.*, vol. 53, pp. 1555–1558, Oct. 1984.
- [27] J. Hebling, K.-L. Yeh, M. C. Hoffmann, and K. A. Nelson, "High-power THz generation, THz nonlinear optics, and THz nonlinear spectroscopy," *IEEE J. Sel. Topics Quantum Electron.*, vol. 14, no. 2, pp. 345–353, Mar./Apr. 2008.
- [28] R. L. Sutherland, *Handbook of Nonlinear Optics*. New York: Marcel Dekker, 2003, Ch. 2.
- [29] D. Grischkowsky, S. Keiding, M. van Exter, and Ch. Fattinger, "Far-infrared time-domain spectroscopy with terahertz beams of dielectrics and semiconductors," *J. Opt. Soc. Amer. B*, vol. 7, pp. 2006–2015, Oct. 1990.
- [30] K. Kawase, J. Shikata, H. Minamide, K. Imai, and H. Ito, "Arrayed silicon prism coupler for a terahertz-wave parametric oscillator," *Appl. Opt.*, vol. 40, no. 9, pp. 1423–1426, Mar. 2001.
- [31] H. Ito, K. Suizu, T. Yamashita, T. Sato, and A. Nawahara, "Random frequency accessible broad tunable terahertz-wave source using phase-matched 4-dimethylamino-N-methyl-4-stilbazolium tosylate crystal," *Jpn. J. Appl. Phys.*, vol. 46, no. 11, pp. 7321–7324, Nov. 2007.
- [32] K. Suizu, T. Shibuya, S. Nagano, T. Akiba, K. Edamatsu, H. Ito, and K. Kawase, "Pulsed high peak power millimeter wave generation via difference frequency generation using periodically poled lithium niobate," *Jpn. J. Appl. Phys.*, vol. 46, no. 40, pp. L982–L984, Oct. 2007.
- [33] K. Suizu, Y. Suzuki, Y. Sasaki, H. Ito, and Y. Avetisyan, "Surface-emitted terahertz-wave generation by ridged periodically poled lithium niobate and enhancement by mixing of two terahertz waves," *Opt. Lett.*, vol. 31, no. 7, pp. 957–959, Apr. 2006.
- [34] Y. Sasaki, Y. Suzuki, K. Suizu, H. Ito, S. Yamaguchi, and M. Imaeda, "Surface-emitted terahertz-wave difference-frequency generation in periodically poled lithium niobate ridge-type waveguide," *Jpn. J. Appl. Phys.*, vol. 45, pp. L367–L369, Mar. 2006.
- [35] J. K. Wahlstrand and R. Merlin, "Cherenkov radiation emitted by ultrafast laser pulses and the generation of coherent polaritons," *Phys. Rev. B*, vol. 68, pp. 054301-1–12, Aug. 2003.
- [36] D. H. Jundt, "Temperature-dependent Sellmeier equation for the index of refraction, n_e , in congruent lithium niobate," *Opt. Lett.*, vol. 22, pp. 1553–1555, Oct. 1997.
- [37] L. Pálfalvi, J. Hebling, J. Kuhl, A. Peter, and K. Polgar, "Temperature dependence of the absorption and refraction of Mg-doped congruent and stoichiometric LiNbO_3 in the THz range," *J. Appl. Phys.*, vol. 97, pp. 123505-1–6, Jun. 2005.
- [38] P. E. Powers, R. A. Alkuwari, J. W. Haus, K. Suizu, and H. Ito, "Terahertz generation with tandem seeded optical parametric generators," *Opt. Lett.*, vol. 30, pp. 640–642, 2005.
- [39] Y. Avetisyan, Y. Sasaki, and H. Ito, "Analysis of THz-wave surface-emitted difference-frequency generation in periodically poled lithium niobate waveguide," *Appl. Phys. B*, vol. 73, pp. 511–514, Nov. 2001.
- [40] Y. Sasaki, Y. Avetisyan, K. Kawase, and H. Ito, "Terahertz-wave surface-emitted difference frequency generation in slant-stripe-type periodically poled LiNbO_3 crystal," *Appl. Phys. Lett.*, vol. 81, no. 18, pp. 3323–3325, Oct. 2002.
- [41] Y. Sasaki, H. Yokoyama, and H. Ito, "Surface-emitted continuous-wave terahertz radiation using periodically poled lithium niobate," *Electron. Lett.*, vol. 41, no. 12, pp. 712–713, Feb. 2005.
- [42] Y. J. Ding, "Efficient generation of high-frequency terahertz waves from highly lossy second-order nonlinear medium at polariton resonance under transverse-pumping geometry," *Opt. Lett.*, vol. 35, pp. 262–264, Jan. 2010.

- [43] Y. Avetisyan, "Terahertz-wave surface-emitted difference-frequency generation without quasi-phase-matching technique," *Opt. Lett.*, vol. 35, pp. 2508–2510, Aug. 2010.
- [44] Y. J. Ding, "Efficient generation of far-infrared radiation from a periodically poled LiNbO₃ waveguide based on surface-emitting geometry," *J. Opt. Soc. Amer. B.*, vol. 28, pp. 977–981, May 2011.
- [45] Y. Sasaki, Y. Avetisyan, H. Yokoyama, and H. Ito, "Surface-emitted terahertz-wave difference frequency generation in two-dimensional periodically poled lithium niobate," *Opt. Lett.*, vol. 30, no. 21, pp. 2927–2929, Nov. 2005.
- [46] J. Shikata, K. Kawase, K. Karino, T. Taniuchi, and H. Ito, "Tunable terahertz-wave parametric oscillators using LiNbO₃ and MgO: LiNbO₃ crystals," *IEEE Trans. Microw. Theory Tech.*, vol. 48, pp. 653–661, Apr. 2000.
- [47] H. Uchida, H. Ochiai, K. Suizu, T. Shibuya, and K. Kawase, "Improving the laser-induced-damage tolerance characteristics of 4-Dimethylamino-N-methyl-4-stilbazoliumtosylate crystals for THz wave generation by annealing," *Jpn. J. Appl. Phys.*, vol. 51, pp. 022601.1–022601.4, Jan. 2012.
- [48] K. Suizu, K. Miyamoto, T. Yamashita, and H. Ito, "High-power terahertz-wave generation using DAST crystal and detection using mid-infrared power-meter," *Opt. Lett.*, vol. 32, pp. 2885–2887, Oct. 2007.
- [49] T. Taniuchi, S. Ikeda, S. Okada, and H. Nakanishi, "Tunable sub-terahertz wave generation from an organic DAST crystal," *Jpn. J. Appl. Phys.*, vol. 44, pp. L652–L654, May 2005.
- [50] J. Hebling, A. G. Stepanov, G. Almasi, B. Bartal, and J. Kuhl, "Tunable THz pulse generation by optical rectification of ultrashort laser pulses with tilted pulse fronts," *Appl. Phys. B.*, vol. 78, pp. 593–599, Mar. 2004.
- [51] D. E. Zelmon, D. L. Small, and D. Jundt, "Infrared corrected Sellmeier coefficients for congruently grown lithium niobate and 5 mol.% magnesium oxide-doped lithium niobate," *J. Opt. Soc. Amer. B.*, vol. 14, pp. 3319–3322, Dec. 1997.
- [52] S. B. Bodrov, A. N. Stepanov, M. I. Bakunov, B. V. Shishkin, I. E. Ilyakov, and R. A. Akhmedzhanov, "Highly efficient optical-to-terahertz conversion in a sandwich structure with LiNbO₃ core," *Opt. Express*, vol. 17, pp. 1871–1879, Feb. 2009.
- [53] D. M. Mittleman, R. H. Jacobsen, and M. G. Nuss, "T-ray imaging," *IEEE J. Sel. Topics Quantum Electron.*, vol. 2, no. 3, pp. 679–692, Sep. 1996.
- [54] D. M. Mittleman, S. Hunshe, L. Boivin, and M. G. Nuss, "T-ray tomography," *Opt. Lett.*, vol. 22, pp. 904–906, Jun. 1997.
- [55] A. J. Fitzgerald, B. E. Cole, and P. F. Taday, "Nondestructive analysis of tablet coating thickness using terahertz pulsed imaging," *J. Pharm. Sci.*, vol. 94, pp. 177–183, Jan. 2005.
- [56] T. Yasui, T. Yasuda, K. Sawanaka, and T. Araki, "Terahertz paintmeter for noncontact monitoring of thickness and drying progress in a paint film," *Appl. Opt.*, vol. 44, pp. 6849–6856, Nov. 2005.
- [57] D. Huang, E. A. Swanson, C. P. Lin, J. S. Schuman, W. G. Stinson, W. Chang, M. R. Hee, T. Flotte, K. Gregory, C. A. Puliafito, and J. G. Fujimoto, "Optical coherence tomography," *Science*, vol. 254, pp. 1178–1181, Nov. 1991.
- [58] J. Takayanagi, S. Kanamori, K. Suizu, M. Yamashita, T. Ouchi, S. Kasai, H. Ohtake, H. Uchida, N. Nishizawa, and K. Kawase, "Generation and detection of broadband coherent terahertz radiation using 17-fs ultrashort pulse fiber laser," *Opt. Express*, vol. 16, pp. 12859–12865, Aug. 2008.



Kei Takeya was born in Boston, MA, in 1975. He received the B.S. degree in physics from Kwansei Gakuin University, Nishinomiya, Japan, in 2002, the M.S. degree from Osaka University, Osaka, Japan, in 2004, and the Ph.D. degree in science from Osaka University.

He was a Postdoctoral Fellow at the Institute of Laser Engineering, Osaka University, from 2007 to 2011. In 2011, he moved to the Department of Electrical Engineering, Nagoya University, Nagoya, Japan.

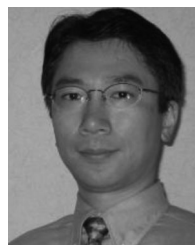
He is currently an Assistant Professor at Kawase Laboratory, Nagoya University. His current research interests include terahertz spectroscopy of hydrogen-bonding materials and terahertz generation from nonlinear optical crystals.

Dr. Takeya is a member of the Japanese Society of Applied Physics.

Koji Suizu was born in Fukuoka, Japan, in 1974. He received the B.S. degree in physics, and the M.S. and Ph.D. degrees in applied physics from Kyushu University, Fukuoka, Japan, in 1996, 1998, and 2001, respectively.

In 2001, he joined the Tera-Photonics Project of the Photo Dynamics Research Center (PDC), RIKEN, Sendai, Japan. In 2003, he was a Research Associate with the Research Institute of Electrical Communication, Tohoku University, Sendai. In 2006, he joined the Department of Electrical Engineering, Nagoya University, Nagoya, Japan, where he was an Assistant Professor. In 2011, he joined the Department of Electrical, Electronics and Computer Engineering, Chiba Institute of Technology, Chiba, Japan, where he is currently an Associate Professor.

Hironobu Sai, photograph and biography not available at the time of publication.



Toshihiko Ouchi received the B.S. degree in electrical and electronic engineering, the M.S. degree in physical electronics, and the Ph.D. degree from the Tokyo Institute of Technology, Tokyo, Japan, in 1986, 1988, and 2002, respectively.

In 1988, he joined Canon Inc., Tokyo, Japan, where he was involved in the development of semiconductor lasers, optical communications, and interconnects. From 2004 to 2008, he held the additional post of the Team Leader in Riken, where he worked on terahertz biological sensing. He is currently the Leader of terahertz devices and imaging system developments in Canon Inc.

Dr. Ouchi is a member of the Japanese Society of Applied Physics and the Optical Society of America.



Kodo Kawase (M'02) was born in Kyoto, Japan, in 1966. He received the B.S. degree from Kyoto University, Kyoto, and the M.S. and Ph.D. degrees from Tohoku University, Sendai, Japan, in 1989, 1992, and 1996, respectively, all in electronic engineering.

In 1998, he was an Assistant Professor at Tohoku Gakuin University, Sendai. In 1999, he became a Subteam Leader at Photo Dynamics Research Center, RIKEN, Sendai. Thereafter, he was a Leader of Kawase Initiative Research Unit at RIKEN, in 2001.

During 2004, he was a Professor in the Graduate School of Agricultural Science, Tohoku University. Since July 2005, he has been a Professor in the Graduate School of Engineering, Nagoya University, Nagoya, Japan, and also affiliated with RIKEN. His current research interests include THz-wave generation and its applications.